Micromechanic modeling and analysis of unsteady-state granular flow in a cylindrical hopper

H.P. ZHU and A.B. YU

Centre for Simulation and Modelling of Particulate Systems, School of Materials Science and Engineering, The University of New South Wales, Sydney, NSW 2052, Australia

Abstract. This paper presents a numerical study of the micro- and macro-dynamic behavior of the unsteady-state granular flow in a cylindrical hopper with flat bottom by means of a modified discrete-element method (DEM) and an averaging method. The results show that the trends of the distributions of the microscopic properties such as the velocity and forces, and the macroscopic properties such as the velocity, mass density, stress and couple stress of the unsteady-state hopper flow are similar to those of steady-state hopper flow, and do not change much with the discharge of particles. However, the magnitudes of the macroscopic properties in different regions have different rates of variation. In particular, the magnitudes of the two normal stresses vary little with time in the orifice region, but decrease in other regions. The magnitude of the shear stress decreases with time when far from the bottom wall and central axis of the hopper. The results also indicate that DEM can capture the key features of the granular flow, and facilitated with a proper averaging method, can also generate information helpful to the test and development of an appropriate continuum model for granular flow.

Key words: average method, discrete-element method, granular flow, hopper flow

1. Introduction

Granular materials are quite common in nature and in industry, appearing as, for example, sands, soil, cement, grains, chemical powders, coal, mineral rocks and so on. The study of the fundamentals of these kinds of materials is essential in order to generate a method for solving a wide range of scientific and technological problems in various fields [1,2]. Computer simulation provides a cost-effective alternative to physical experimentation to achieve this goal.

In general, granular material is a discrete system whose physical properties are discontinuous with respect to position and time. Therefore, it can be described by a discrete model on an individual particle scale, which can generate detailed information about the micro-dynamic behavior of the granular material. A major type of discrete model is based on the so-called Discrete Element Method (DEM) originally proposed by Cundall and Strack [3]. In the method, the motion of every particle is traced and the gradients of translation and rotation of a particle are determined in terms of the forces and the torques exerted on it. DEM-based simulation has been recognized as an effective method to study the fundamentals of granular materials [4–9].

Granular material can also be described by a continuum model in an average sense. In the continuum description, the macroscopic behavior of granular flow is described by the balance equations facilitated with constitutive relations and boundary conditions. In the past, two continuum models developed within the framework of plasticity theory and kinetic theory of molecular dynamics have extensively been used to study the dynamic behavior of granular materials [10,11], [12, pp. 1–46], [13, Chapters 6, 7, 9]. They have been shown to be applicable

to quasi-static and rapid flow regimes, respectively. However, they do not satisfactorily apply to a system in which different flow regimes coexist such as hopper flow. An alternative approach is the combined approach of a discrete method and an averaging method, which takes into account the discrete nature of granular materials without any global assumption, thus allowing a better understanding of the fundamental mechanisms of granular flow [14–17]. In the approach, supported by a proper averaging method, the macroscopic quantities, such as density, velocity and stress can be obtained in terms of the microscopic quantities, such as velocities of particles and interaction forces and torques between particles.

In this paper, the three-dimensional granular flow in a cylindrical hopper with flat bottom is investigated with a modified DEM and an averaging method. The modified DEM and the averaging method used in this work are first briefly described. The microscopic properties directly related to the velocity and forces of particles in the hopper flow are then examined. Finally, the macroscopic properties, such as velocity, mass density, stress and couple stress are investigated. The proper use of the weighting function in the averaging method is also discussed.

2. Mathematical models

2.1. DISCRETE-ELEMENT METHOD

In the DEM simulation, a granular material is modeled based on a finite number of discrete, semi-rigid spherical or polygon-shaped particles interacting by means of contact or non-contact forces, and the translational and rotational motions of every single particle in a considered system are described by Newton's laws of motion. For simplicity, our present study is limited to granular systems only composed of spherical particles, in which the effect of interstitial fluid and non-contact forces, such as the van der Waals and electrostatic forces, can be ignored. Therefore, the governing equations for translational and rotational motion of particle i can be given by

$$m_i \frac{\mathrm{d}\mathbf{v}_i}{\mathrm{d}t} = \sum_j \mathbf{f}_{ij} + m_i \mathbf{g}, \tag{1}$$

$$I_i \frac{\mathrm{d}\omega_i}{\mathrm{d}t} = \sum_j \mathbf{m}_{ij}, \tag{2}$$

where $\mathbf{v}_i$, ω_i are, respectively, the translational and angular velocities of particle i with mass m_i and moment of inertia I_i. The forces involved are the gravitational force, $m_i \mathbf{g}$, and interaction force $\mathbf{f}_{ij}$ between particles due to the plastic and elastic deformation resulting from particle collision, sliding and rolling. Further, $\mathbf{m}_{ij}$ is the torque acting on particle i by particle j arising from their interaction.

In general, the total interaction force between particles i and j, $\mathbf{f}_{ij}$, can be expressed as a normal component, $\mathbf{f}_{ij}^n$, and a tangential one, $\mathbf{f}_{ij}^t$. Various approaches have been proposed to model $\mathbf{f}_{ij}^n$ and $\mathbf{f}_{ij}^t$. One of the most popular force models was developed based on the consideration of contact elastic force and viscous contact damping force [4,7–9]. The normal force includes elastic and damping components, whilst the tangential force includes frictional and damping components. The normal elastic force, $\mathbf{f}_{ij}^{ne}$, described by the Hertz theory [18, pp. 84–106], can be given by

$$\mathbf{f}_{ij}^{ne} = \frac{4}{3} E_i^* \sqrt{R_{ij}^*} \left(\delta_{ij}^n \right)^{3/2} \mathbf{n}_{ij}, \tag{3}$$

where E_i^* and R_{ij}^* are the reduced modulus of elasticity and particle radius, δ_{ij}^n is the relative normal displacement at contact, and $\mathbf{n}_{ij}$ is the unit contact vector. E_i^*, R_{ij}^*, δ_{ij}^n and $\mathbf{n}_{ij}$, are, respectively, given by $E_i^* = E_i/[2(1-v_i^2)]$, $R_{ij}^* = (R_i R_j)/(R_i + R_j)$, $\delta_{ij}^n = R_i + R_j - |\mathbf{r}_j - \mathbf{r}_i|$, and $\mathbf{n}_{ij} = (\mathbf{r}_i - \mathbf{r}_j)/|\mathbf{r}_i - \mathbf{r}_j|$, where E_i and v_i are the modulus of elasticity and Poisson's ratio of particle i; R_i and R_j are the radii of particles i and j, and $\mathbf{r}_i$ and $\mathbf{r}_j$ are the position vectors of particles i and j. The normal damping force, $\mathbf{f}_{ij}^{nd}$, which is modeled as a dashpot that dissipates a proportion of the relative kinetic energy, is given by

$$\mathbf{f}_{ij}^{nd} = -c_{ij}^n \left(8 m_{ij} E_i^* \sqrt{R_{ij}^* \delta_{ij}^n} \right)^{1/2} \left(\mathbf{v}_{ij} \cdot \mathbf{n}_{ij} \right) \mathbf{n}_{ij}, \tag{4}$$

where c_{ij}^n is the normal damping coefficient, $\mathbf{v}_{ij}$ is the relative velocity of particles i and j at contact, given by $\mathbf{v}_{ij} = \mathbf{v}_i - \mathbf{v}_j + \omega_i \times \mathbf{C}_{ij} - \omega_j \times \mathbf{C}_{ji}$, $\mathbf{v}_i$ and $\mathbf{v}_j$ are the velocities of particle i and j, and $\mathbf{C}_{ij}$ is a vector from the mass center of the particle to the contact point.

The frictional component of the tangential force is given by

$$\mathbf{f}_{ij}^{te} = -\mu_{ij} \left| \mathbf{f}_{ij}^{ne} \right| \left(1 - \left(1 - \min \left(\left| \mathbf{v}_{ij}^t \right|, \delta_{ij}^{max} \right)/\delta_{ij}^{max} \right)^{3/2} \right) \hat{\mathbf{v}}_{ij}^t, \tag{5}$$

where μ_{ij} is the sliding friction coefficient between particles i and j, $\hat{\mathbf{v}}_{ij}^t = \mathbf{v}_{ij}^t/|\mathbf{v}_{ij}^t|$, $\mathbf{v}_{ij}^t$ is the vector of the relative tangential displacement of particles i and j, and δ_{ij}^{max} is the relative tangential displacement when the sliding starts, given by $\delta_{ij}^{max} = \mu_{ij}\delta_{ij}^n(2-v_i)/[2(1-v_i)]$. Equation (5) suggests that the friction is described by the theory proposed by Mindlin and Deresiewicz [19] prior to the sliding (*i.e.*, when $|\mathbf{v}_{ij}^t| < \delta_{ij}^{max}$) and the Coulomb friction model when the particles at contact start to slide relatively. The tangential damping force is given by

$$\mathbf{f}_{ij}^{td} = 2 c_{ij}^t \left(1{\cdot}5 \mu_{ij} m_{ij} \left| \mathbf{f}_{ij}^{ne} \right| \sqrt{1 - |\mathbf{v}_{ij}^t|/\delta_{ij}^{max}}/\delta_{ij}^{max} \right)^{1/2} (\mathbf{v}_{ij} \times \mathbf{n}_{ij}) \times \mathbf{n}_{ij}, \tag{6}$$

where c_{ij}^t is the tangential damping coefficient. Note that (6) implies that, when sliding occurs, there is no contribution of the tangential damping to the tangential force.

In general, the contact between two spheres is not at a single point but is a finite area due to the deformation of both spheres. The inter-particle forces act over the contact region between particles i and j, rather than the mass center of the particle, and they will generate a torque, $\mathbf{m}_{ij}$. The torque $\mathbf{m}_{ij}$ causing particle i to rotate is contributed by the tangential and normal components of the traction distribution, $\mathbf{m}_{ij}^t$ and $\mathbf{m}_{ij}^n$, respectively. Implemented in a discrete simulation, $\mathbf{m}_{ij}^t$ is usually expressed as

$$\mathbf{m}_{ij}^t = \mathbf{C}_{ij} \times \mathbf{f}_{ij}^t. \tag{7}$$

For many inelastic bodies such as viscoelastic particles, the normal traction distribution on the contact area between two contacting particles is asymmetrical due to the relative rotation of particles. The asymmetry leads to a non-zero torque, $\mathbf{m}_{ij}^n$, given by

$$\mathbf{m}_{ij}^n = -\min \left\{ \mu_{r,ij} \left| \mathbf{f}_{ij}^n \right|, \mu_{r,ij}' \left| \omega_{ij}^n \right| \right\} \hat{\omega}_{ij}^n, \tag{8}$$

where $\mu_{r,ij}$ is the rolling friction coefficient, $\mu_{r,ij}'$ is the rotational stiffness and $\hat{\omega}_{ij}^n = \omega_{ij}^n/|\omega_{ij}^n|$, ω_{ij}^n is the component of the vector of the relative angular velocity of particles i and j in their contact plane. The vector $\mathbf{m}_{ij}^n$ is often referred to as the rolling friction torque which provides a resistance to relative rolling motion between particles [20–22].

2.2. AVERAGING METHOD

By use of a proper averaging procedure, the discrete system considered above can be transferred into a corresponding continuum system. Assume that the mass density ρ, the velocity $\mathbf{u}$, the angular velocity ω are respectively

$$\rho = \int_{T_t} \sum_i h_i m_i \, \mathrm{d}s, \tag{9}$$

$$\mathbf{u} = \frac{1}{\rho} \int_{T_t} \sum_i h_i m_i \mathbf{v}_i \, \mathrm{d}s, \tag{10}$$

$$\omega = \frac{1}{\lambda} \int_{T_t} \sum_i h_i I_i \omega_i \, \mathrm{d}s, \tag{11}$$

where $h_i = h(\mathbf{r}_i - \mathbf{r}, s - t)$, $h = h(\mathbf{r}, t)$ is the weighting function, which is positive in the limited domain $\Omega = \left\{ (\mathbf{r},t) \,\middle|\, \mathbf{r} \in \Omega_p \subset R^3, t \in T_t \subset R \right\}$ and zero otherwise. The variables $\mathbf{r}$ and t are, respectively, the position vector and time to which the average value of the considered quantities is assigned, and $\lambda = \int_{T_t} \sum_i h_i I_i \, \mathrm{d}s$. Differentiating ρ, $\rho \mathbf{u}$ and $\lambda \omega$ by use of Equations (1), (2), (9–11), we can obtain the balance equations of mass and linear momentum and angular momentum of the continuum system, respectively given by [16,17]

$$D(\rho) + \rho \nabla \cdot \mathbf{u} = 0, \tag{12}$$

$$D(\rho \mathbf{u}) + \rho \mathbf{u} \nabla \cdot \mathbf{u} = \nabla \cdot \mathbf{T} + \rho \mathbf{g}, \tag{13}$$

$$D(\lambda \omega) + \lambda \omega \nabla \cdot \mathbf{u} = \nabla \cdot \mathbf{M} + \mathbf{M}', \tag{14}$$

where $D(\cdot)$ represents the material derivative of a tensor. Further, $\mathbf{T}$ is the stress tensor, $\mathbf{M}$ is the couple-stress tensor, and $\mathbf{M}'$ is the rate of supply of internal spin to particles, respectively given by

$$\mathbf{T} = -\int_{T_t} \sum_i h_i m_i \mathbf{v}'_i \otimes \mathbf{v}'_i \, \mathrm{d}s + \int_{T_t} \sum_i \sum_{j>i} g_{ij} \mathbf{d}_{ij} \otimes \mathbf{f}_{ij} \, \mathrm{d}s, \tag{15}$$

$$\mathbf{M} = -\int_{T_t} \sum_i h_i I_i \mathbf{v}'_i \otimes \omega_i \, \mathrm{d}s + \frac{1}{2} \int_{T_t} \sum_i \sum_{j>i} g_{ij} \mathbf{d}_{ij} \otimes (\mathbf{m}_{ij} - \mathbf{m}_{ji}) \, \mathrm{d}s, \tag{16}$$

$$\mathbf{M}' = \frac{1}{2} \int_{T_t} \sum_i \sum_{j>i} (\mathbf{m}_{ij} + \mathbf{m}_{ji})(h_i + h_j) \, \mathrm{d}s \tag{17}$$

where $\mathbf{v}'_i = \mathbf{v}_i - \mathbf{u}$ is the fluctuant velocity of particle i with respect to the average velocity, $\mathbf{d}_{ij}$ is the part of the branch vector connecting the mass centers of particles i and j within domain Ω_p; g_{ij} is the weighting coefficient determined by the weighting function $h(\mathbf{r}, t)$, given by $g_{ij} = \int_0^1 h(\bar{\mathbf{r}}_i + r\mathbf{d}_{ij} - \mathbf{r}, s - t) \mathrm{d}r$, $\bar{\mathbf{r}}_i = \mathbf{r}_i$ if $\mathbf{r}_i - \mathbf{r} \in \Omega_p$; otherwise, $\bar{\mathbf{r}}_i$ is the position vector of the point of intersection of vector $\mathbf{d}_{ij}$ and boundary $\partial \Omega_p$ of domain Ω_p.

A particle may collide with a wall. Therefore, the interaction between particles and walls should be included in the continuum description. The contribution of the interaction between particles and walls to stress and couple stress can be given by

$$\mathbf{T}^b = \int_{T_t} \sum_i g_i^b \mathbf{d}_i^b \otimes \mathbf{f}_i^b \, \mathrm{d}s, \tag{18}$$

and

$$\mathbf{M}^b = \int_{T_t} \sum_i g_i^b \mathbf{d}_i^b \otimes \mathbf{m}_i^b \, \mathrm{d}s,$$ (19)

where $\mathbf{d}_i^b$ is the ray from the center of mass of particle i to boundary $\partial\Omega_p$ of domain Ω_p, via a point on the wall and perpendicular to the tangential plane of the point; g_i^b is the weighting coefficient corresponding to walls, given by $g_i^b = \int_0^1 g(\mathbf{r}_i + r\mathbf{d}_i^b - \mathbf{r}, s - t)\mathrm{d}r$. Equations (9–11), (15–19) give the relationship between microscopic and macroscopic quantities of granular materials.

The microscopic dynamic behavior of granular flows is often described in Cartesian coordinates in DEM simulation. However, for granular flows with a geometry such as a cylindrical hopper, it is more convenient to describe their macroscopic dynamic behavior in orthogonal curvilinear coordinates. Therefore, it is necessary to determine the transformation between the variables under the two coordinates. For this reason, let $\{x^i\}$ be the Cartesian coordinates of the three-dimensional Euclidian space R^3, $\{y^i\}$ ($y^i = y^i(x^1, x^2, x^3)$, $i = 1, 2, 3$) be the orthogonal curvilinear coordinates in this space, u, ω, T and M be the coordinates of the macroscopic quantities $\mathbf{u}$, ω, $\mathbf{T}$ and $\mathbf{M}$ of granular matter under $\{x^i\}$, and $\bar{u}$, $\bar{\omega}$, $\bar{T}$ and $\bar{M}$ be the coordinates under $\{y^i\}$. It can be readily obtained that

$$\bar{u} = uA, \bar{\omega} = \omega A, \bar{T} = A^\mathrm{T} T A, \bar{M} = A^\mathrm{T} M A.$$ (20)

where $A = (\partial y^i / \partial x^j) \bar{G}$, $\bar{G}$ is 3×3 matrix whose components are $\sqrt{g_{ij}}$ ($i, j = 1, 2, 3$), $g_{ii} = \mathbf{e}'_i \cdot \mathbf{e}'_i = (\partial x^1 / \partial y^i)^2 + (\partial x^2 / \partial y^i)^2 + (\partial x^3 / \partial y^i)^2 (i = 1, 2, 3)$, and $g_{ij} = 0$ if $i \neq j$. Equation (20) gives the expressions of $\mathbf{u}$, ω, $\mathbf{T}$ and $\mathbf{M}$ under the orthogonal curvilinear coordinates $\{y^i\}$.

Cylindrical coordinates are special orthogonal curvilinear coordinates. Assuming that $\{r, \theta, z\}$ is the cylindrical coordinates, we observe that there exists a relationship between cylindrical and Cartesian coordinates, namely

$$x^1 = r\cos\theta, x^2 = r\sin\theta, x^3 = z.$$ (21)

It can be obtained that

$$A = \begin{pmatrix} \cos\theta & -\sin\theta & 0 \\ \sin\theta & \cos\theta & 0 \\ 0 & 0 & 1 \end{pmatrix}.$$ (22)

Therefore, by use of (20) and (22), the expressions of $\mathbf{u}$, ω, $\mathbf{T}$ and $\mathbf{M}$ under the cylindrical coordinates can be readily obtained. Note that the mass density is independent of the coordinate transformation, as it is a scalar.

3. Results and discussion

3.1. SIMULATION CONDITIONS AND MEASUREMENT STRATEGY

To generate results that can be directly compared with those under steady-state flow conditions, the geometry of the hopper used in this work is similar to that in our previous work [9]. It is cylindrical in shape, of diameter of $20d$ (d is the maximum particle diameter) and with a circular orifice of diameter of $8d$ at the center of its flat bottom. Twenty-four thousand multisized spherical particles of uniform size distribution in a range of $0\cdot8 - 1\cdot0d$ are considered. Other physical parameters for particles and wall are as follows. Young's modulus and Poisson ratio of particles are set to $50000\pi\rho_p dg/6$ (ρ_p is the mass density of particle, and g is

the gravitational acceleration) and 0·3, respectively. The sliding and rolling friction coefficients between particles are set to 0·6 and 0·001d, respectively. The normal and tangential damping coefficients are set to 0·3. The wall is assumed to have the same properties as the particles, except the sliding friction coefficient, which is 0·5. The time step used is $0.001\sqrt{d/g}$.

The microscopic properties of granular flows can be generated by means of the DEM simulation, whereas their macroscopic properties can be obtained by use of the micro-dynamic information generated and the average method described above. In this work, the microscopic quantities of the hopper flow, including velocity field and force structure, are analyzed in Cartesian coordinates $\{x, y, z\}$ fixed at the center of the orifice of the hopper with z-axis at the central axis of the hopper. The values of the macroscopic quantities, such as density, velocity, stress and couple stress at the probe point far from the bottom and vertical walls (larger than $4d$) in the coordinates, are calculated by use of Equations (9), (10), (15) and (16), whereas those at the probe point adjacent to the walls by use of Equations (18) and (19) in addition to these equations. Since the resulting macroscopic variables should be reasonably axially symmetric, consistent with the practical treatment [23, pp. 298–372], all computed macroscopic quantities are averaged from the values of two symmetrical points and shown as a function of radius r and height z in cylindrical coordinates. The cylindrical coordinates $\{r, \theta, z\}$ starts at the center of the orifice of the hopper. The velocity, v, mass density, ρ, three independent components of planer stress, T_{zz}, T_{rr} and T_{rz}, and two dominant components of couple stress, $M_{r\theta}$ and $M_{z\theta}$, have been investigated in this coordinate system. Their magnitudes are obtained by means of Equations (20) and (22).

3.2. MICROSCOPIC ANALYSIS

In the DEM simulation, the particles with random initial velocities are first allowed to gradually settle onto the hopper under gravity, giving a packing with height of about $47d$. These particles are then discharged when the hopper outlet is removed, as shown in Figure 1. Three distinct flow patterns are observed. In the upper part, particles flow downward layer by layer except those very near the vertical walls due to the sliding resistance by the walls. In the lower part, particles flow in a V-shape and are discharged except for a small number of particles staying at the bottom corner of the hopper.

The present microscopic analysis is focused on two key aspects: the velocity field and force structure. Since the trajectories of and contact forces acting on individual particles are traced in a DEM simulation, information for such analysis can be readily established. Figure 2
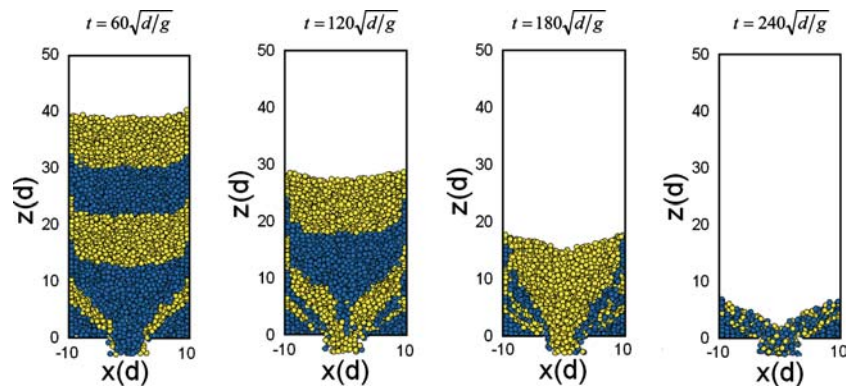

Figure 1. Discharging process of the hopper flow, represented by particles in the central vertical section at different times.
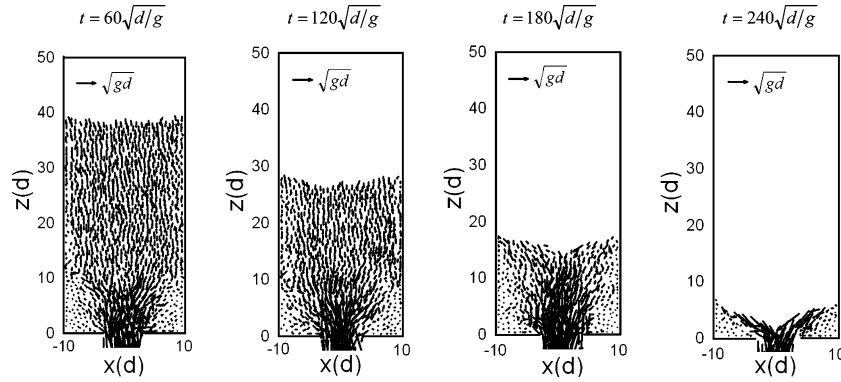
Figure 2. Velocity profiles at different times for particles in the central vertical section.

shows the velocity fields in a vertical mid-section of the hopper at $t = 60\sqrt{d/g}$ (time of discharge), $t = 120\sqrt{d/g}$, $t = 180\sqrt{d/g}$ and $t = 240\sqrt{d/g}$, where each vector represents the components of the velocity of a particle in a section as long as its center is located between $\pm 0.5d$ of the position of the section. It can be seen that, in the upper part, the velocity in the vertical direction dominates and is almost uniform across the hopper, except for a narrow shear zone adjacent to the vertical wall. In the lower part, the particles have much larger velocities at the orifice and very low velocities around the bottom corner of the hopper. Large velocities in the radial direction concentrate at the two sides of the orifice. These results are qualitatively consistent with the previous experimental and numerical observations for such a hopper flow [23–25], [26, pp. 298–372]. That is, there are four different zones: a stagnant zone at the bottom corner of the hopper, a plug flow zone in the upper part, a converging-flow zone in the lower part, and a transition zone from plug flow to converging flow. Moreover, the plug-flow zone is observed to reduce with the discharge of particles, whereas the converging flow zone varies little before $t = 180\sqrt{d/g}$ and then reduces with the discharge of the particles in this zone. The flow regimes can be more clearly shown in terms of the distribution of the averaged velocity in the section on macroscopic analysis.

The force structure is another important local characteristic of granular matter. It has been used to depict the flow structure, force transmission and other dynamic behavior of particles [4, 5, 7, 9]. Figure 3 shows the force network in the vertical mid-section at different times, where the thickness of each stick connecting two particle centers is proportional to
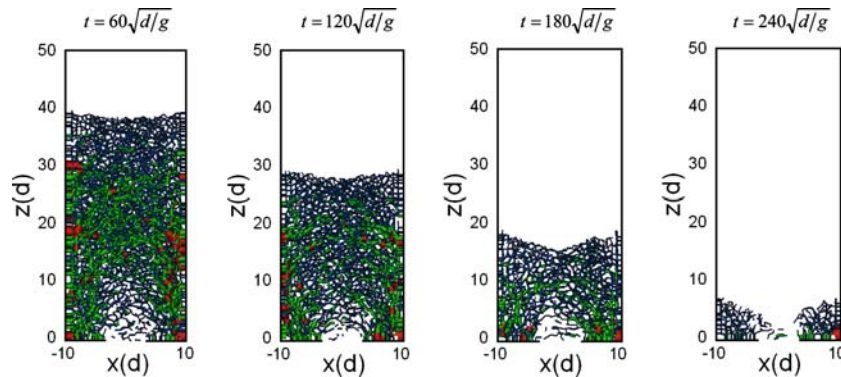

Figure 3. Force networks at different times for particles in the central vertical section.

the magnitude of the force. The normal contact force is probably the most important, as the contact tangential force is related to it and is relatively small. Therefore, only the normal force is included in this figure. Note that the present analysis is focused on the relative values of the contact forces for a given time; different scales have been used for different times for better illustration of the flow and force structures. It can be observed that, similar to the steady-state hopper flow [9], large forces are exerted on the particles at the bottom and vertical walls to support the particles in the top part. The forces gradually propagate from the walls into the particle bed. Relatively large forces are also observed in the middle height of the flow, which corresponds to the transition from plug flow to converging flow in the hopper flow. In the orifice region, the forces are very small and the force chains are broken. A force chain means a connection between particles which confines the relative movement between particles. The breakage of force chains may imply the relative movements between the particles. Therefore, the flow and force structures are related. These characteristics do not change with time.

3.3. MACROSCOPIC ANALYSIS

The DEM results can be used to calculate the macroscopic variables such as mass density, velocity, stress and couple stress according to (9), (10), (15) and (16). However, strictly speaking, these macroscopic quantities depend on the weighting function $h(\mathbf{r}, s)$. Therefore, the selection of a proper weighting function is important in applying the equations formulated above. The need to find a suitable weighting function has been noticed; a weighting function has been recommended, and given by [17]

$$h(\mathbf{r}, s) = f(s)g(\bar{s}),$$ (23)

where $\bar{s} = |\mathbf{r}|$, and $f(s)$ is the simplified S_B distribution function [27], whilst $g(\bar{s})$ is an extension of the univariate distribution to three variants. They can be explicitly written as

$$f(s) = \begin{cases} \frac{1}{\sqrt{2\pi}} \frac{2L_t}{(L_t^2 - s^2)} \exp\left(-\frac{1}{2} \log^2 \frac{L_t + s}{L_t - s}\right), & |s| < L_t \\ 0, & |s| \geq L_t \end{cases},$$ (24)

$$g(\bar{s}) = \begin{cases} \frac{c}{4\pi L_p (L_p^2 - \bar{s}^2)} \exp\left(-\frac{1}{2} \log^2 \frac{L_p + \bar{s}}{L_p - \bar{s}}\right), & \bar{s} < L_p \\ 0, & \bar{s} \geq L_p \end{cases},$$ (25)

where L_t and L_p are the distribution parameters, c is the normalized constant of the distribution function $g(\bar{s})$. The functions $f(s)$ and $g(\bar{s})$ are smooth in the entire space, and decrease monotonically with increasing s and $\bar{s}$, respectively.

Parameter L_p or L_t in the weighting function (23) determines the amount of the contributing particles to a probe point or time, and the magnitude of contribution of every particle as well, as illustrated in Figure 4. The specification of appropriate values of L_p and L_t is a significant part of the application of the averaging method described above. In fact, as shown in Figures 5 and 6, L_p and L_t do not affect the trend of the distribution of velocity and stress (only the vertical velocity and the trace of the stress tensor are shown, since the other components of velocity and stress lead to the same conclusion). However, if L_p and L_t are too small, the resulting macroscopic quantities fluctuate, giving unreasonable average results. On the other hand, if they are too large, the local properties of these quantities may be eliminated. The results in Figures 5 and 6 suggest that, to balance the friction, we can choose $L_p = 4 \cdot 0 d$ and $L_t = 4 \cdot 0 \sqrt{d/g}$. Such a selection can ensure that the averaged quantities smoothly vary in a considered domain and retain the local properties of these quantities as much as possible. The results below were all obtained with these two values.
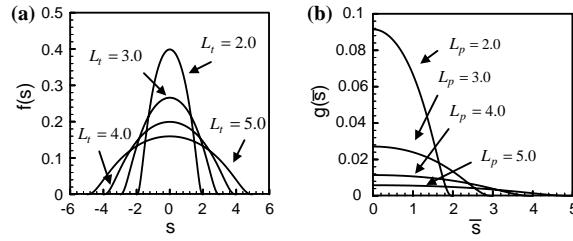
Figure 4. Variation of the weighting function with parameter L_p and L_t: (a) function $f(s)$ and (b) function $g(\bar{s})$.
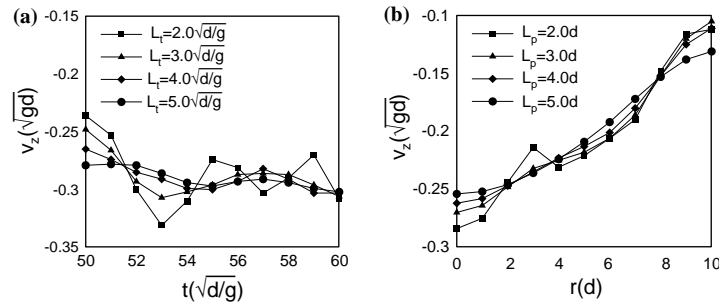

Figure 5. Effect of the parameters in the weighting function on vertical velocity v_z: (a) the variation of v_z with time t for different L_t when $L_p = 4\cdot0d$ for a probing point located at r=0 and $z = 12\cdot0d$ and (b) the variation of v_z with radius r for different L_p when $L_t = 4\cdot0\sqrt{d/g}$ and $t = 50\sqrt{d/g}$ at height $z = 12\cdot0d$.
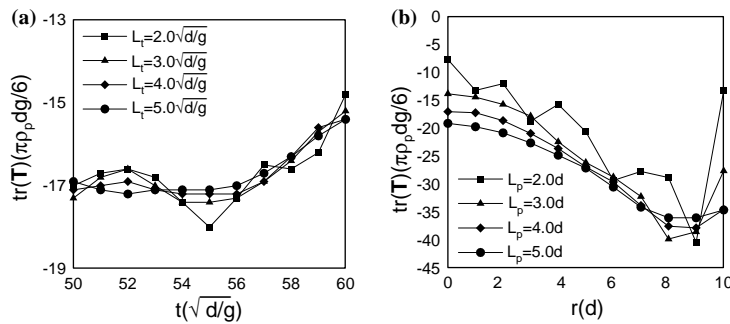

Figure 6. Effect of the parameters in the weighting function on the trace of stress tensor tr(T): (a) the variation of tr(T) with time t for different L_t when $L_p = 4\cdot0d$ for a probing point located at $r = 0$ and $z = 12\cdot0d$; and (b) the variation of tr(T) with radius r for different L_p when $L_t = 4\cdot0\sqrt{d/g}$ and $t = 50\sqrt{d/g}$ at height $z = 12\cdot0d$.

Figure 7 shows the mass density or bulk density profiles at $t = 60\sqrt{d/g}$, $t = 120\sqrt{d/g}$ and $t = 180\sqrt{d/g}$. It can be seen that the mass density is lowest at the orifice and increases away from the orifice in the lower part. The magnitude of mass density in this part does not change much with time. In the upper part, the mass density is almost constant in the central region and, because of the dilatancy that takes place during shearing, decreases with the distance to the axis of the hopper in the region close to the wall. The magnitude of mass density in the central upper part decreases with the discharge of particles. Figure 8 shows the velocity profiles of the hopper flow in the vertical mid-section of the hopper at different times. As expected, the distributions are in agreement with the micro-dynamic analysis as above.

Theoretically, the stress contains two parts: a kinetic contribution related to the transport of particles and a collisional contribution related to the interaction force between particles and between particles and walls. For hopper flow, the stress is attributed mainly to collisions
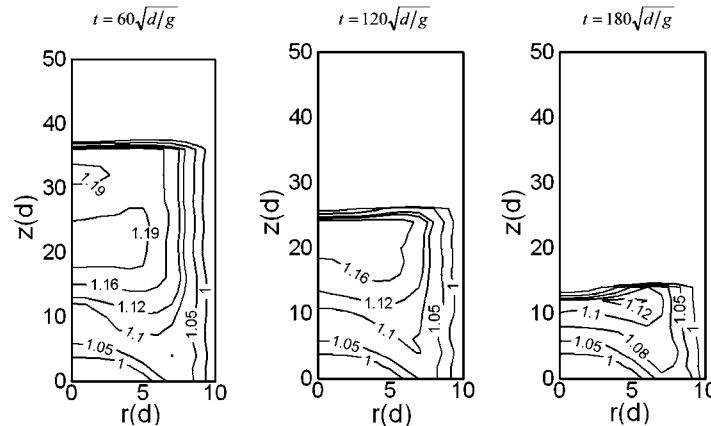
Figure 7. Contour plots of mass density of the unsteady-state hopper flow at different times (the units for mass density are $\pi\rho_p/6$).
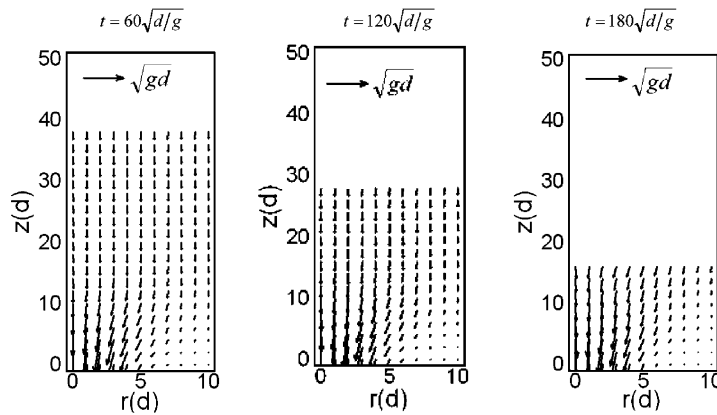

Figure 8. Velocity fields of the unsteady-state hopper flow at different times.

between the particles and between particles and walls. It is related to the magnitude and direction of the interaction forces. However, close to the orifice, the transport of particles may also play a role. To ensure the accuracy of the stress distribution, the two contributions are included in the present calculation. Figure 9 shows the radial distribution of the three components of the stress tensor, that is, two normal stress, T_{zz} and T_{rr}, and a shear stress, T_{rz}. Another shear stress, T_{zr}, has a similar distribution to T_{rz} in the whole domain except in a small region adjacent to the walls, which is not shown for brevity. The results indicate that the distributions of these stresses are similar to those of steady-state hopper flow [28], and have similar trends for different times. It can be observed from Figures 9 (a) and (b) that the two normal stresses are low in a region close to the orifice, and large in a region near the bottom corner. In the upper part, the two stresses vary little in the central section but vary somewhat near the wall. Furthermore, the two normal stresses in this upper part are almost the same in the central region, but not so in a region adjacent to the wall. The magnitude of the radial normal stress T_{rr} is large as well in the middle height in the vertical direction, which is, as expected, in accordance with the force network in Figure 3. As shown in Figure 9(c), the shear stress has its largest magnitude in a region close to the vertical wall and decreases away from this region. In the regions adjacent to the bottom wall and central axis of the hopper, the shear stress is very low. The magnitudes of the two normal stresses vary little with time in
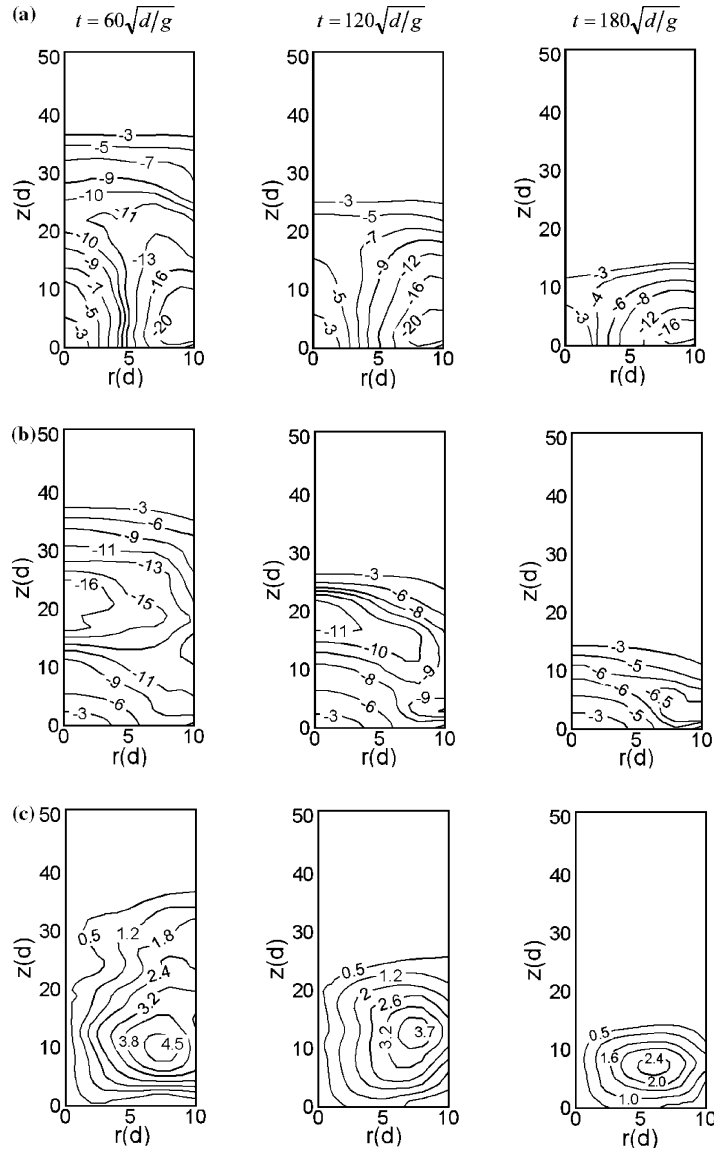
Figure 9. Contour plots of the distribution of stress of the unsteady state hopper flow at different times (the units for stress are $\pi\rho_p dg/6$): (a) T_{zz}; (b) T_{rr} and (c) T_{rz}.

the orifice region, but decrease in other regions. The magnitude of the shear stress decreases with time at locations far from the bottom wall and central axis of the hopper.

For steady-state hopper flow, the most dominant components in the couple stress are $M_{r\theta}$ adjacent to the vertical wall of the hopper and $M_{z\theta}$ close to the bottom wall [28]. This phenomenon has also been observed in the present simulation of unsteady-state hopper flow, as shown in Figure 10, where the distributions of the two dominant components at different times are given. In general, the couple stresses at points far from a wall result from the transport of particles and the collisions between particles. Close enough to the wall they will also be affected by the collisions between particles and wall. The observed sharp increase of the magnitudes of $M_{r\theta}$ and $M_{z\theta}$ in Figure 10 can be attributed to the effect of the vertical and bottom walls. The fluctuation of the couple stress far from the walls results mainly from
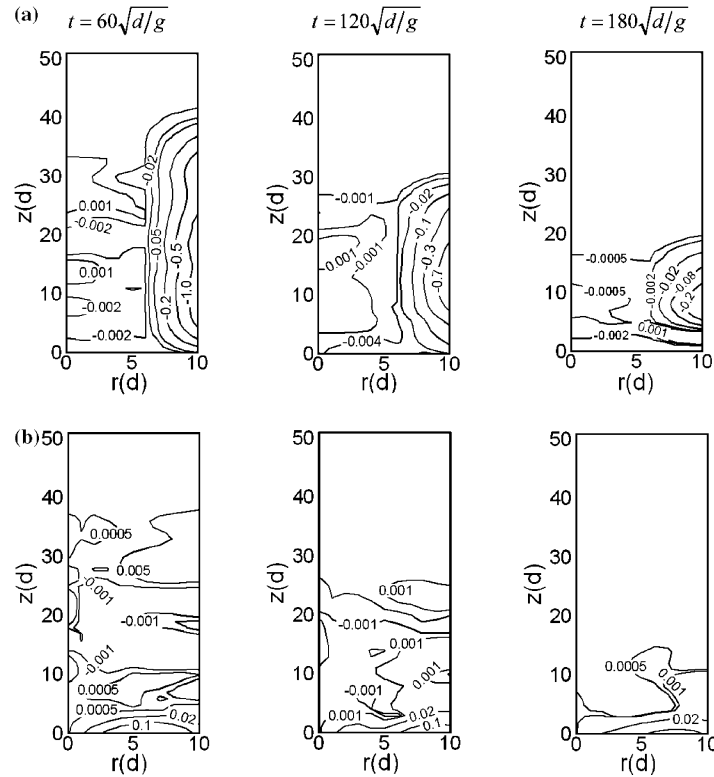
Figure 10. Contour plots of the distribution of couple stress of the unsteady-state hopper flow at different times (the units for couple stress are $\pi \rho_p d^2 g / 6$): (a) $M_{r\theta}$ and (b) $M_{z\theta}$.

collisions between particles. The width or height of the region with a large magnitude of $M_{r\theta}$ or $M_{z\theta}$ is almost the same for different times, that is $4d$ for $M_{r\theta}$ and $2d$ for $M_{z\theta}$. These facts indicate that the couple stress related to the gradient of particle rotation should be considered when the effect of walls is included, which highlights the complexity of the macro-dynamic analysis of granular flow adjacent to physical boundaries.

4. Conclusions

A numerical investigation of the micro- and macro-dynamic behavior of the unsteady-state granular flow in a cylindrical hopper with flat bottom has been carried out by means of a modified DEM and an averaging method. It has been found that there are four distinct flow zones in the hopper: stagnant, plug flow, converging flow and transition zone from plug flow to converging flow. The plug flow zone reduces with time, while the converging flow zone varies little and then reduces with the discharge of the particles from this zone. Force arching in the flow is strong and related to the flow structure of particles. The trends of the distributions of the macroscopic properties, such as the velocity, mass density, stress and couple stress of the hopper flow, are similar to those of steady-state hopper flow. They do not vary much with time. However, the magnitudes of these properties in different regions vary at different rates. In particular, the magnitudes of the two normal stresses vary little with time in the orifice region, but decrease in other regions; the magnitude of the shear stress decreases with discharge of particles when far from the bottom wall and central axis of the hopper, and the width or height of the region with a large magnitude of $M_{r\theta}$ or $M_{z\theta}$ is almost the same for

different times. These results about macroscopic properties should be useful in formulating and testing continuum models of hopper flow.

Acknowledgements

References

1. P.G. de Gennes, Granular matter: a tentative view. *Rev. Mod. Phys.* 71 (1999) 374–382.
2. S.F. Edwards and D.V. Grinev, Transmission of stress in granular materials as a problem of statistical mechanics. *Physica A* 302 (2001) 162–186.
3. P.A. Cundall and O.D.L. Strack, A discrete numerical model for granular assemblies. *Geotechnique* 29 (1979) 47–65.
4. P.A. Langston, U. Tüzün and D.M. Heyes, Discrete element simulation of internal stress and flow fields in funnel flow hoppers. *Powder Technol.* 85 (1995) 153–169.
5. R. Gutfraind and O. Pouliquen, Study of the origin of shear zones in quasi-state vertical chute flows by using discrete particle simulations. *Mech. Mat.* 24 (1996) 273–285.
6. P.W. Cleary and M.L. Sawley, DEM modeling of industrial granular flows: 3D case studies and the effect of particle shape on hopper discharge. *Appl. Math. Model.* 26 (2002) 89–111.
7. K. Tanaka, M. Nishida, T. Kunimochi and T. Takagi, Discrete element simulation and experiment for dynamic response of two-dismensional granular matter to the impact of a spherical projectile. *Powder Technol.* 124 (2002) 160–173.
8. A.B. Yu, DEM-an effective method for particulate matter. In: *Discrete Element Methods: Numerical Modeling of Discontinua*. Virginia: Ameriacan Society of Civil Engineers (2002) pp. 17–22.
9. H.P. Zhu and A.B. Yu, Steady-state granular flow in a 3D cylindrical hopper with flat bottom using DEM simulation: microscopic analysis. *J. Phys. D, Appl. Phys.* 37 (2004) 1497–1508.
10. C.K.K. Lun, S.B. Savage, D.J. Jeffrey and N. Chepurniy, Kinetic theories for granular flow: inelastic particles in Couette flow and slightly inelastic particles in a general flowfield. *J. Fluid Mech.* 140 (1984) 223–256.
11. C.S. Campbell, Rapid granular flows. *Annu. Rev. Fluid Mech.* 22 (1990) 57–92.
12. R.M. Nedderman, *Statics and Kinematics of Granular Materials*. New York: Cambridge University Press (1992) 352 pp.
13. W. Powrie, *Soil Mechanics: Concepts and Applications*. London: E & FN Spon (1997) 420 pp.
14. O.R. Walton and R.L. Braun, Viscosity, granular-temperature, and stress calculations for shearing assemblies of inelastic, frictional disks. *J. Rheology* 30 (1986) 949–980.
15. Y. Zhang and C.S. Campbell, The interface between fluid-like and solid-like behaviour in two-dimensional granular flows. *J. Fluid Mech.* 237 (1992) 541–568.
16. M. Babic, Average balance equations for granular materials. *Int. J. Eng. Sci.* 35 (1997) 523–548.
17. H.P. Zhu and A.B. Yu, Averaging method of granular materials. *Phys. Rev. E* 66 (2002) 021302.
18. K.L. Johnson, *Contact Mechanics*. Cambridge, UK: Cambridge University Press (1985) 452 pp.
19. R.D. Mindlin and H. Deresiewicz, Elastic spheres in contact under varying oblique forces. *J. Appl. Mech.* 20 (1953) 327–344.
20. K. Iwashita and M. Oda, Rolling resistance at contacts in the simulation of shear band development by DEM. *J. Engrg. Mech., ASCE* 124 (1998) 285–292.
21. A. Tordesillas and S. Walsh, Incorporating rolling resistance and contact anisotropy in micromechanical models of granular media. *Powder Technol.* 124 (2002) 106–111.
22. H.P. Zhu and A.B. Yu, The effects of wall and rolling resistance on the couple stress of granular materials in vertical flow. *Physica A* 325 (2003) 347–360.
23. J.P.K. Seville, U. Tüzün and R. Clift, *Processing of Particulate Solids,* Landon: Blackie Academic and Professional (1997) 372 pp.
24. G.P. Deutsch and L.C. Schmidt, Pressures on silo walls. *J. Engrg. Industry, ASME, Series B* 91 (1969) 450–459.
25. U. Tüzün, G.T. Houlsby, R.M. Nedderman and S.B. Savage, The flow of granular-materials - 2. velocity distributions in slow flow. *Chem. Eng. Sci.* 37 (1982) 1691–1709.

26. H. Sakaguchi and F. Ozaki, Analysis of the formation of arches plugging the flow of granular Materials. In: C. Thornton (ed.), *Powders and Grains*. Rotterdam: A.A. Balkema (1993) 351–355.

27. N.L. Johnson, Systems of frequency curves generated by methods of translation, *Biometrika* 36 (1949) 149–176.

28. H.P. Zhu and A.B. Yu, Steady-state granular flow in a 3D cylindrical hopper with flat bottom using DEM simulation: macroscopic analysis. (2004) (submitted).